




Article

Partially Yttria-Stabilized Zirconia Crystals Co-Doped with Neodymium, Cerium, Terbium, Erbium or Ytterbium Oxides

Mikhail A. Borik ¹, Alexey V. Kulebyakin ¹ , Elena E. Lomonova ¹ , Filipp O. Milovich ^{1,2,*} ,
Valentina A. Myzina ¹, Polina A. Ryabochkina ³, Natalia Y. Tabachkova ^{1,2}, Natalia V. Sidorova ³
and Artem S. Chislov ^{1,2}

¹ Prokhorov General Physics Institute of the Russian Academy of Sciences, 119991 Moscow, Russia; borik@lst.gpi.ru (M.A.B.); kulebyakin@lst.gpi.ru (A.V.K.); lomonova@lst.gpi.ru (E.E.L.); vamyzina@lst.gpi.ru (V.A.M.); ntabachkova@misis.ru (N.Y.T.); chislov.artem@bk.ru (A.S.C.)

² Department of Materials Science of Semiconductors and Dielectrics, National University of Science and Technology "MISIS", 119049 Moscow, Russia

³ Laboratory of Optical Spectroscopy of Laser Materials, Ogarev Mordovia State University, 430005 Saransk, Russia; Ryabochkina@freemail.mrsu.ru (P.A.R.); ya.natalka2112@yandex.ru (N.V.S.)

* Correspondence: philippmilovich@gmail.com

Abstract: In this work, we studied the phase composition, local structure and mechanical characteristics of ZrO₂ crystals partially stabilized with Y₂O₃ and co-doped with Nd₂O₃, CeO₂, Er₂O₃, Tb₂O₃ and Yb₂O₃. Crystals were grown by directional melt crystallization in a cold container. The phase composition and structure of crystals were studied by X-ray diffractometry and transmission electron microscopy. The study of the features of the incorporation of rare-earth cations with different ionic radii into the transformable (t) and nontransformable (t') tetragonal phases was carried out by the method of selective laser spectroscopy and time-resolved spectroscopy. Mechanical characteristics such as microhardness and fracture toughness were studied by the indentation method. It is shown that the phase composition and structure of crystals at the same total concentration of doping oxides depends on the degree of substitution of Y³⁺ cations by rare-earth cations. Rare earth ions of the beginning of the lanthanide series predominantly occupy positions in the nontransformable tetragonal phase of crystals based on zirconium dioxide. Ions of the end of a series of lanthanides do not show selectivity when entering the transformable (t) phase and nontransformable (t') phase. The study of the mechanical characteristics of the crystals showed that the values of fracture toughness increase with an increase in the ionic radius of the rare earth element of the co-doped oxide, while the values of the microhardness of the crystals slightly decrease.

Keywords: partially stabilized zirconia; anisotropy mechanical properties; skull melting; solid solutions



Citation: Borik, M.A.; Kulebyakin, A.V.; Lomonova, E.E.; Milovich, F.O.; Myzina, V.A.; Ryabochkina, P.A.; Tabachkova, N.Y.; Sidorova, N.V.; Chislov, A.S. Partially Yttria-Stabilized Zirconia Crystals Co-Doped with Neodymium, Cerium, Terbium, Erbium or Ytterbium Oxides. *Crystals* **2021**, *11*, 1587. <https://doi.org/10.3390/cryst11121587>

Academic Editors: Jun Tan and Quan Dong

Received: 19 November 2021

Accepted: 16 December 2021

Published: 20 December 2021

Publisher's Note: MDPI stays neutral with regard to jurisdictional claims in published maps and institutional affiliations.



Copyright: © 2021 by the authors. Licensee MDPI, Basel, Switzerland. This article is an open access article distributed under the terms and conditions of the Creative Commons Attribution (CC BY) license (<https://creativecommons.org/licenses/by/4.0/>).

1. Introduction

Partially stabilized zirconia materials possess high strength, microhardness and fracture toughness and are chemically and biologically inert refractory materials with good heat insulating properties. Partially stabilized zirconia ceramic materials are widely used in engineering as construction ceramics, heat insulating coatings and in medicine [1–6]. They possess a wide range of mechanical properties which depend on the composition and structure of the material. Solid state sintering techniques are used both for the synthesis of conventional ZrO₂-based industrial ceramics (heaters, heat insulating ceramics, crucibles, radio engineering components, etc.) and for the production of high-strength high-ductility construction ceramics (engine components, oxygen sensors, solid state electrolytes, bioceramics, etc.). A necessary condition for the synthesis of bioceramics is a close-to-zero residual porosity of the material.

There are various techniques of the production of high-density ceramics, e.g., high-temperature sintering, high-pressure sintering, hot pressing, isostatic cold pressing, microwave sintering, etc. The efficiency of a technology is judged based on residual porosity

which is a measure of the deviation of the material's density from the theoretical one. Advanced techniques of sintering from ultrafine charge with a highly homogeneous grain size of ~10–200 nm allow one to obtain high-strength materials with a high density (85–98% of the theoretical one) that are resistant to degradation [7–17]. A specific feature of the ceramic materials is a random pattern of the distribution of raw charge components and various defects in their structure potentially providing for a large scatter in the properties of the material. Furthermore, the presence of grain boundaries delivers a substantial contribution to the physicochemical properties of these materials and their destruction mechanisms. The mechanical properties of these materials depend on the type and concentration of stabilizing oxides and the type of doping oxides that are introduced in low concentrations for the improvement of the performance and/or stability of properties of the materials under operation conditions [18–20]. Thus, the mechanical properties of the partially stabilized ceramics on the basis of zirconia are largely affected by the synthesis technique, raw material properties and process conditions. These parameters determine not only the structure and phase composition of the materials that are related to their properties but also the sizes of the crystalline grains in the ceramic material, the homogeneity of their composition and also the extension and composition of the grain boundaries. The contribution of these factors to the mechanical parameters of the ceramics is quite tangible.

Single crystal partially stabilized zirconia are grown using directional melt crystallization [21–24]. Study of single crystals can ignore some factors related to grain boundaries and determine the contribution of the type and concentration of stabilizing oxides on the structure, phase composition and mechanical properties of partially stabilized zirconia single crystals.

The aim of this work is to study the effect of the ionic radius of doping oxide cations (Nd, Ce, Eu, Er and Yb) on the phase transformations, structure and properties of $\text{ZrO}_2\text{--Y}_2\text{O}_3$ -based solid solution single crystals.

2. Materials and Methods

$\text{ZrO}_2\text{--Y}_2\text{O}_3\text{--R}_2\text{O}_3$ solid solution single crystals ($\text{R} = \text{Nd, Ce, Er, Tb, Yb}$) were obtained by directed crystallization of the melt in a cold container. The crystallization rate was 10 mm/h. As initial components, powders of Zr, Y, Nd, Ce, Er, Tb and Yb oxides (China) were used. The raw powders (main component content of at least 99.99%) were preliminarily mechanically stirred and loaded into the crucible. Initial melting was carried out with metallic zirconium. After melting the melt container was mechanically driven out from the heating zone at a 5 mm/h speed. The cross-section and height of the as-grown single crystals were 5 to 20 mm and 30 to 40 mm, respectively.

The phase composition of the single crystals was determined using X-ray diffraction with a Bruker D8 diffractometer. The test wafers for the phase composition study were cut out from the single crystals perpendicularly to the $\langle 100 \rangle$ axis. Since the reflection intensity of single crystals is far higher than that of polycrystals, (100) plane reflection allows simultaneous detection of reflections from different phases on one wafer cut, these reflections being separated at high angles of $2\Theta \sim 130^\circ$. The phase fraction was determined from the intensity of the diffraction peaks which was normalized to the integral reflection coefficient for different phases.

The transmittance spectra were recorded on a Lambda 950 Perkin Elmer spectrometer at $T = 300\text{ K}$. The absorption spectra of the $^4\text{I}_{9/2} \rightarrow ^4\text{F}_{3/2}$ transition of the Nd^{3+} ions, the $^4\text{I}_{15/2} \rightarrow ^4\text{S}_{3/2}$ transition of the Er^{3+} ions and the $^2\text{F}_{7/2} \rightarrow ^2\text{F}_{5/2}$ transition of the Yb^{3+} ions at $T = 77\text{ K}$ were recorded in a single-beam setup with an MDR-23 monochromator fitted with a set of diffraction gratings for operation in the 200–2000 nm range. The radiation source was an incandescent halogen lamp.

The radiation source for the recording of the luminescence spectra for the $^4\text{F}_{3/2} \rightarrow ^4\text{I}_{9/2}$ transition of the Nd^{3+} ions at $T = 77\text{ K}$ was an 800 nm semiconductor laser with a 10 nm bandwidth. Non-selective luminescence spectra of Er^{3+} ions were recorded with excitation by a luminescent diode. A $\text{Al}_2\text{O}_3\text{:Ti}$ crystal laser was used for the selective laser excitation

of Er^{3+} and Yb^{3+} ions. The wavelength range of fundamental frequency sweep for the laser used was 700 to 980 nm and for the second harmonic, 350–490 nm. The spectral bandwidth was within 0.05 nm. The excitation pulse duration was 10–15 ns. The excitation source for the time-delay luminescence spectra of Er^{3+} ions was the second harmonic of a YAG:Nd laser ($\lambda = 532$ nm). The time delay and the time lapse for luminescence spectra recording were set with an SR250 boxcar average. The time delay was varied within 2 to 200 μs and the time lapse was set to 15 μs . Depending on the recording spectral range the radiation detectors were FEU-79 and FEU-89 photomultipliers for the 400–1200 nm spectral sensitivity range and an FD-7G photodiode for the 800–1700 nm spectral sensitivity range. The luminescence extinction kinetics was recorded with a GDS-820 C digital oscilloscope.

To obtain the true luminescence spectra of rare-earth ions in the test single crystals, we calibrated the resultant spectra to allow for the spectral sensitivity of the instrument.

The structure of the crystals was studied using transmission electron microscopy under a JEM-2100 microscope at a 200 kV accelerating voltage.

The microhardness and fracture toughness were measured using microindentation on a DM8 B AUTO microhardness tester and a Wolpert Hardness Tester 930 with a four-face diamond Vickers pyramid.

The microhardness tests were conducted at a 3 N load with K_{1c} being calculated for a 100 N load. K_{1c} for Palmqvist type cracks was calculated using the Nihara Equation (1):

$$K_{1c} = 0.035 \left(\frac{L}{a} \right)^{-\frac{1}{2}} \left(\frac{CE}{H} \right)^{2/5} H a^{1/2} C^{-1} \quad (1)$$

where K_{1c} is the tension intensity coefficient, $\text{MPa} \cdot \text{m}^{-1/2}$; L is the length of the radial crack, m; a is the indentation half width, m; E is Young's modulus, Pa; H is the hardness and Pa; C is the relation of the hardness H to the yield stress σ . For zirconia-based materials $C = H/\sigma \approx 3$ [3].

3. Results and Discussion

To evaluate the effect of additionally introduced cations (Nd, Ce, Er, Tb, Yb and Sc) on the ZrO_2 – Y_2O_3 solid solutions, the total concentrations of the stabilizing (Y_2O_3) and doping (Nd_2O_3 , CeO_2 , Er_2O_3 , Tb_2O_3 and Yb_2O_3) oxides were varied from 2.8 to 3.2 mol.% since high fracture toughness was obtained earlier in this Y_2O_3 concentration range for the ZrO_2 – Y_2O_3 system [25]. The crystal compositions are hereinafter denoted as $x\text{Y}_y\text{RSZ}$ where x and y are the concentrations of the stabilizing (Y_2O_3) and doping (Nd_2O_3 , CeO_2 , Er_2O_3 , Tb_2O_3 and Yb_2O_3) oxides in mol.%, respectively. The Y_2O_3 concentration in the test solid solutions was 2 or 2.5 mol.%. The concentration of the doping oxides varied within 0.5 to 1.2 mol.%.

Crystals doped with various impurities had a columnar shape characteristic of directional crystallization of the melt. The crystals were non-transparent, their color being similar regardless of doping impurity type. Figure 1 shows the appearance of 2.0Y0.8RSZ crystals where $R = \text{Nd, Ce, Er, Tb and Yb}$.

The phase composition of the crystals was studied using X-ray diffraction on a BrukerD8 instrument for wafers cut from the crystals perpendicularly to the $\langle 100 \rangle$ direction. From all the test crystal compositions, only the 2.0Y0.8NdSZ specimen was a single-phase tetragonal one. Other crystals contained two tetragonal phases, t and t' , having different tetragonality degrees. Table 1 shows the phase composition, weight ratio of phases and tetragonality degree of the test crystals.

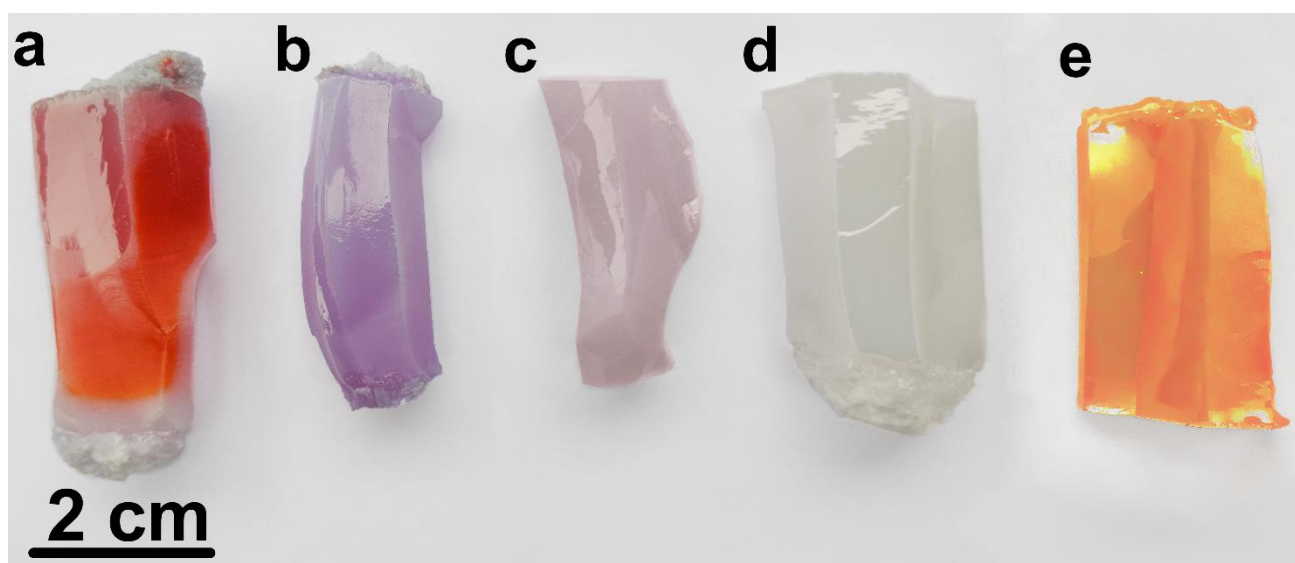


Figure 1. Appearance of (a) 2.0Y0.8CeSZ, (b) 2.0Y0.8NdSZ, (c) 2.0Y0.8ErSZ, (d) 2.0Y0.8YbSZ and (e) 2.0Y0.8TbSZ crystals.

Table 1. Phase composition and tetragonality degree of crystals.

Specimen	Phase	R = Ce		R = Nd		R = Tb		R = Er		R = Yb	
		Wt, %	c/√2a	Wt, %	c/√2a	Wt, %	c/√2a	Wt, %	c/√2a	Wt, %	c/√2a
2.0Y0.8RSZ	t	95(5)	1.015	100(5)	1.016	90(5)	1.015	90(5)	1.015	90(5)	1.015
	t'	5(5)	1.008	-	-	10(5)	1.006	10(5)	1.007	10(5)	1.008
2.5Y0.5RSZ	t	90(5)	1.015	90(5)	1.015	85(5)	1.015	85(5)	1.015	85(5)	1.0145
	t'	10(5)	1.0065	10(5)	1.006	15(5)	1.007	15(5)	1.006	15(5)	1.007
2.5Y0.7RSZ	t	90(5)	1.015	90(5)	1.015	85(5)	1.015	85(5)	1.015	85(5)	1.0145
	t'	10(5)	1.007	10(5)	1.006	15(5)	1.007	15(5)	1.007	15(5)	1.0075
2.0Y1.2RSZ	t	-	-	-	-	75(5)	1.015	70(5)	1.0145	70(5)	1.014
	t'	-	-	-	-	25(5)	1.004	30(5)	1.007	30(5)	1.006

The tetragonal phase with a high degree of tetragonality (t) is responsible for the transformation hardening of the material, since it is subject to stress-induced tetragonal to monoclinic transition. The second tetragonal phase (t') is non-transformable and does not contribute to this hardening mechanism.

The data summarized in Table 1 suggest that the tetragonality degree of the phases depends on the concentration of stabilizing oxides to a lesser extent in comparison with binary systems. An important factor for zirconia stabilization with two oxides is the substitution of stabilizing oxide cations (Y) for doping oxide cations (Nd, Ce, Er, Tb and Yb) in the solid solution. For an equal total concentration of 3.2 mol.% the quantity of the transformable phase is significantly lower in the 2.0Y1.2RSZ specimens in comparison with the 2.5Y0.7RSZ specimens (R = Er, Yb, Tb and Sc). The use of doping with two stabilizing oxides allowed the retention of the quantity and tetragonality degree of the transformable phase at levels comparable with those for the 2.8YSZ specimens which exhibited the highest fracture toughness for the YSZ system [25]. Changes in the parameters of the crystal structure at constant Y₂O₃ concentrations in solid solutions are related to the ionic radius of the co-doping cations and, probably, with their position in the lattice sites of t and t' tetragonal phases. The incorporation of rare-earth elements (Nd³⁺, Er³⁺ and Yb³⁺) with different ionic radii into the t and t' phases was studied using selective laser spectroscopy and time resolution spectroscopy.

Figure 2 shows the ⁴F_{3/2} → ⁴I_{9/2} transition luminescence spectra of Nd³⁺ ions for Nd³⁺ ion ⁴F_{5/2} level excitation at T = 77 K for the 2Y0.8NdSZ, 2.5Y0.5NdSZ and 2.5Y0.7NdSZ concentration range of the crystals. The luminescence spectrum of the cubic 10Y0.5NdSZ single crystal is shown for comparison.

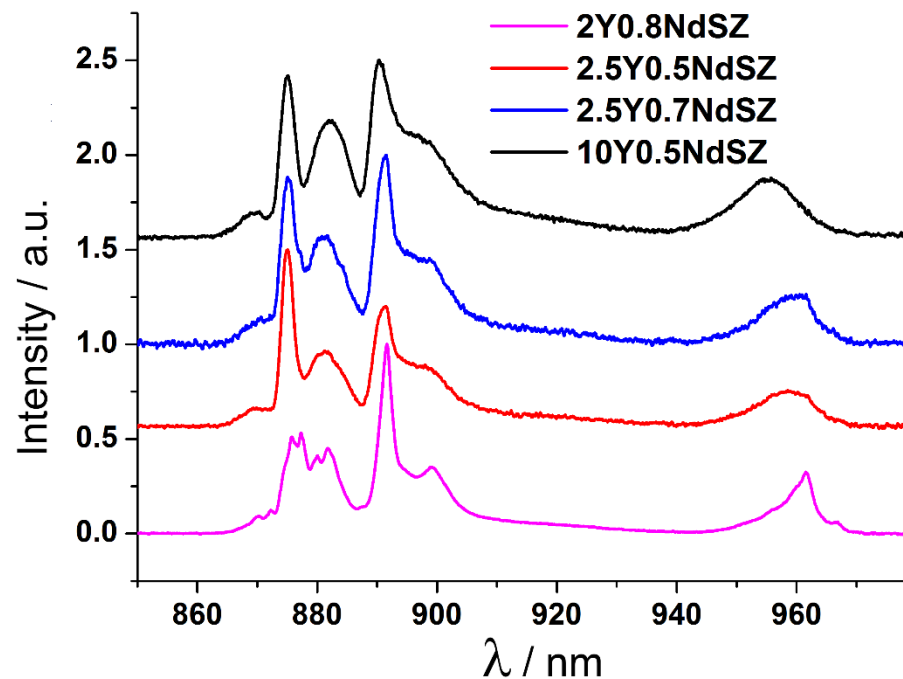


Figure 2. Luminescence spectra of Nd^{3+} ions for the ${}^4\text{F}_{3/2} \rightarrow {}^4\text{I}_{9/2}$ transition ${}^4\text{F}_{5/2}$ level excitation for YNdSZ single crystals for ${}^4\text{F}_{5/2}$ level excitation with a 800 nm semiconductor laser at $T = 77$ K.

Comparison of the luminescence spectra of Nd^{3+} ions in the YNdSZ crystals showed that the luminescence spectrum pattern of the 2.0Y0.8NdSZ crystal that contains only one phase differs from the luminescence spectra of the 2.5Y0.5NdSZ and 2.5Y0.7NdSZ crystals which have a tetragonal structure and contain the t and t' phases. For most tetragonal crystals containing the t and t' phases, the shapes of the spectral bands are close to that for the luminescence spectrum of the cubic 10Y0.5NdSZ zirconia crystal. Since the tetragonality degree of the transformable phase is close to unity ($c/\sqrt{2}a \sim 1.006$), and taking into account that the Nd^{3+} ions have a larger ionic radius than the Y^{3+} ions it was concluded that the crystals co-doped with neodymia contain predominantly Nd^{3+} optical centers in the non-transformable tetragonal phase. The pattern of the spectral bands of these centers is close to that of the bands in the spectra of cubic zirconia crystals, differing only in the splitting magnitude of the top Stark sublevel of the main ${}^4\text{I}_{9/2}$ state.

Thus, the results above suggest that for the 2.5Y0.5NdSZ and 2.5Y0.7NdSZ crystals which contain the t and t' phases, Nd^{3+} ions are predominantly contained in the non-transformable phase.

In order to study the parameters of the optical centers for ions in the end of the lanthanide series (Er^{3+} , Yb^{3+}) which have smaller ionic radii, absorption and luminescence spectra of Er^{3+} ions for the 2Y0.8ErSZ, 2.5Y0.5ErSZ and 2.5Y0.7ErSZ crystals containing the t and t' phases were recorded and the parameters of the spectra were compared with those of the respective spectra for the cubic 10Y0.5ErSZ crystal.

The absorption spectra of the 2Y0.8ErSZ, 2.5Y0.5ErSZ and 2.5Y0.7ErSZ crystals corresponding to the transition from the main ${}^4\text{I}_{15/2}$ multiplet to the excited ${}^4\text{S}_{3/2}$ multiplet at $T = 77$ K are shown in Figure 3.

The patterns of the absorption spectra for the 2Y0.8ErSZ, 2.5Y0.5ErSZ and 2.5Y0.7ErSZ crystals are similar. For the 10Y0.5ErSZ crystal, the absorption center transforms: the band near 542.1 nm and the asymmetrical band near 542.4 nm are replaced for an asymmetrical band peaking at 542.7 nm.

For a more detailed study of the formation of the optical centers in these crystals, the ${}^4\text{S}_{3/2} \rightarrow {}^4\text{I}_{15/2}$ transition luminescence spectra of Er^{3+} ions were recorded with selective excitation to the ${}^4\text{F}_{7/2}$ level of Er^{3+} ions by radiation in the 439 to 446 nm range with a 1 nm step. The excitation luminescence spectra for excitation with $\lambda_{\text{ex}} = 440$ nm and

$\lambda_{\text{ex}} = 445$ nm for the 2Y0.8ErSZ, 2.5Y0.5ErSZ, 2.5Y0.7ErSZ and 10Y0.5ErSZ crystals are shown in Figure 4.

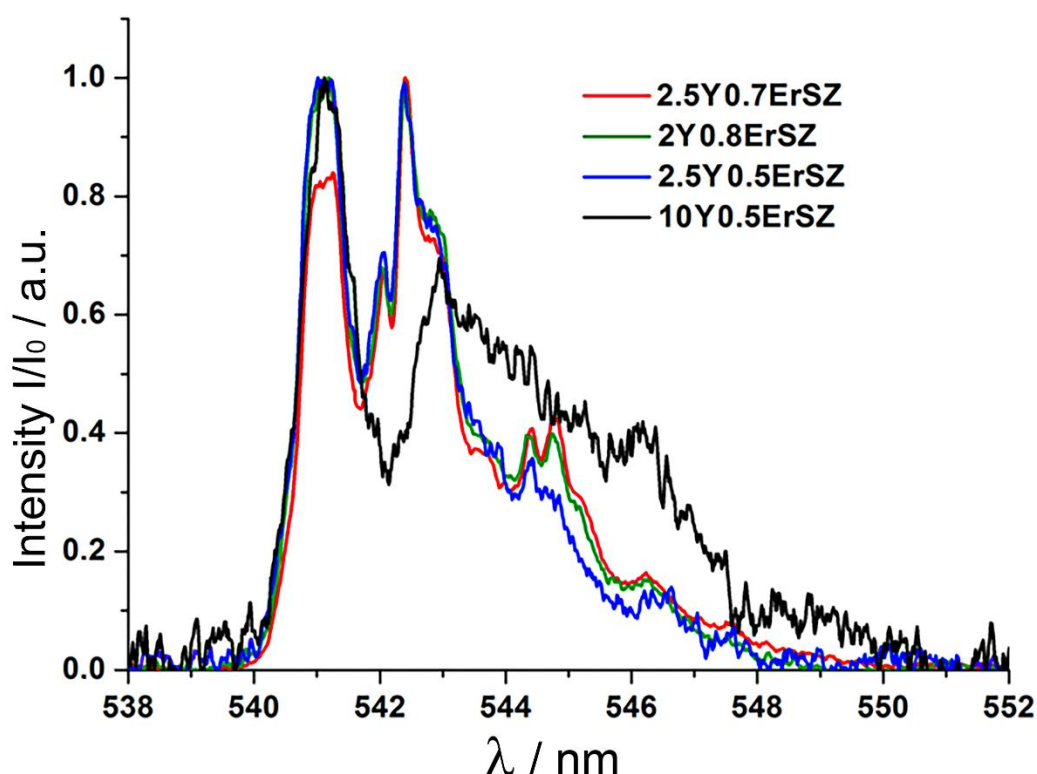


Figure 3. Absorption spectra of the 2Y0.8ErSZ, 2.5Y0.5ErSZ and 2.5Y0.7ErSZ crystals corresponding to the transition from the main multiplet $^4I_{15/2}$ to the excited multiplet $^4S_{3/2}$ at $T = 77$ K.

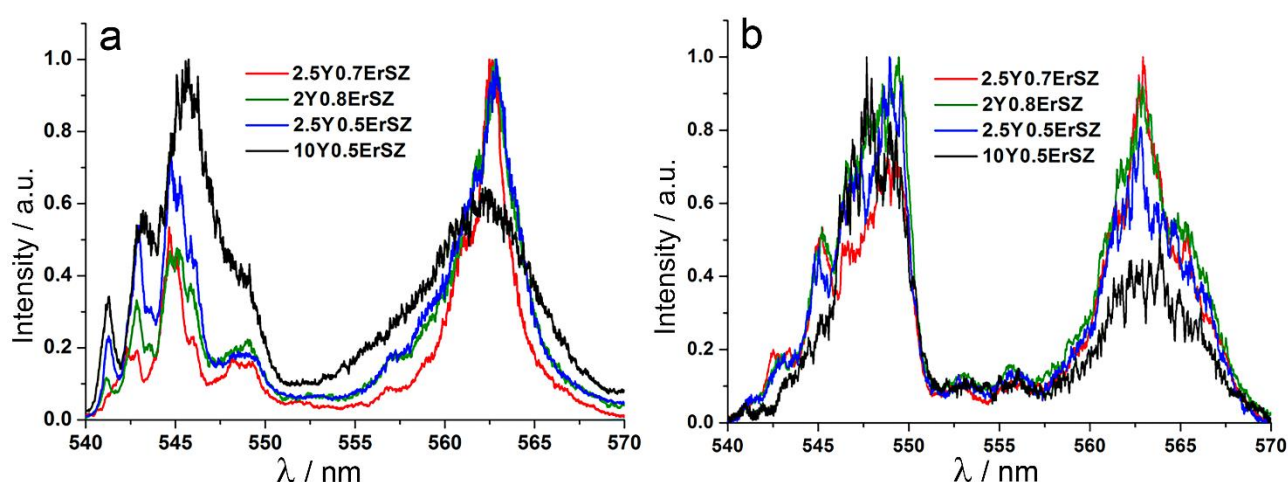


Figure 4. $^4S_{3/2} \rightarrow ^4I_{15/2}$ transition luminescence spectra of Er^{3+} ions for selective excitation to the $^4F_{7/2}$ level at $T = 77$ K. (a) $\lambda_{\text{ex}} = 440$ nm and (b) $\lambda_{\text{ex}} = 445$ nm.

For all the test crystals, a change in the excitation wavelength leads to a noticeable transformation of the luminescence spectrum patterns. Excitation at 440 nm mainly produces bands at 540–545 nm whereas excitation at 445 nm makes bands in the 546–550 nm range clearer. This indicates the presence of different optical centers of Er^{3+} ions in the crystals, these optical centers differing in the symmetry of their local crystalline neighborhood.

The fact that the bands in the 540–545 nm and 546–550 nm regions correspond to Er^{3+} optical centers with different local neighborhood symmetry is further supported by

the results of luminescence extinction kinetics analysis for the $^4S_{3/2}$ level of Er^{3+} ions in the 2.5Y0.5ErSZ crystal as shown in Figure 5. The luminescence extinction curves were recorded at $\lambda_{rec} = 545$ nm and $\lambda_{rec} = 549$ nm at excitation by the second harmonic of a $\lambda = 532$ nm YAG:Nd laser.

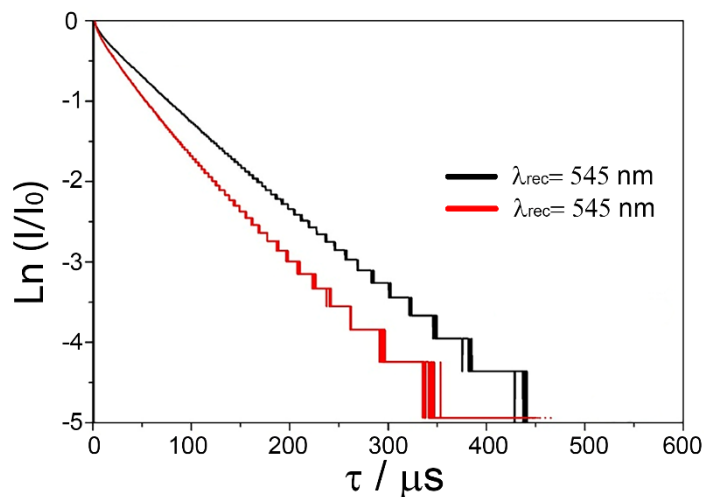


Figure 5. Luminescence extinction kinetics analysis for the $^4S_{3/2}$ level of Er^{3+} ions in the 2.5Y0.5ErSZ single crystal.

The non-exponential pattern of the luminescence extinction curves for the $^4S_{3/2}$ level recorded at different excitation wavelengths suggests the presence of several types of Er^{3+} ion optical centers in the specimen. The times in which luminescence intensity declines by e times which are equal to 70 and 55 μs as determined from the decomposition curves recorded at 545 and 549 nm suggest the presence of Er^{3+} ion optical centers with different local neighborhood in the 2.5Y0.5ErSZ crystal. Er^{3+} ions with a lower local neighborhood symmetry exhibit shorter lifetime ($\tau = 55$ μs). For Er^{3+} ion optical centers whose local neighborhood does not contain anion vacancies, the crystalline field will be distorted to a lesser extent and their lifetime will be longer ($\tau = 80$ μs).

Experimental data on the luminescent spectral properties of the 2Y0.8ErSZ, 2.5Y0.5ErSZ and 2.5Y0.7ErSZ crystals did not reveal any indications of selective incorporation of Er^{3+} ions into the t and t' phases. The predominant factor controlling the formation of Er^{3+} ion optical centers in all the test crystals is the presence oxygen vacancies in the neighborhood of rare-earth ions.

Yb^{3+} ions follow Er^{3+} ions in the lanthanide series and mark the end of the lanthanide series. The Yb^{3+} ionic radius is smaller than the Er^{3+} one.

The structure of the Stark levels of the $^2F_{7/2}$ and $^2F_{5/2}$ multiplets of Yb^{3+} ions is shown in Figure 6. The red arrow corresponds to the transition between the lower Stark level of the $^2F_{7/2}$ multiplet and the lower Stark level of the $^2F_{5/2}$ multiplet of Yb^{3+} ions. The blue arrow corresponds to the transition between the lower Stark level of the $^2F_{5/2}$ multiplet and the lower Stark level of the $^2F_{7/2}$ multiplet of Yb^{3+} ions.

Previously, the spectral-luminescent properties of crystals of yttrium-stabilized zirconium dioxide doped with Yb^{3+} ions were studied in [26]. The authors of this work discriminate in the spectra of crystals of cubic stabilized zirconia doped with Yb^{3+} ions, characteristic lines in the absorption and luminescence spectra, designated by them as A, B, and C, due to transitions between the lower Stark levels of the $^2F_{7/2}$ and $^2F_{5/2}$ multiplets of Yb^{3+} ions (Figure 6). Line A corresponds to Yb^{3+} ions occupying positions in the center of the oxygen eight-vertex. Line B corresponds to Yb^{3+} ions located in the center of an eight-vertex structure and having a vacancy in the second coordination sphere. Line C belong to Yb^{3+} ions occupying positions in the center of the seven-vertex formed by oxygen ions.

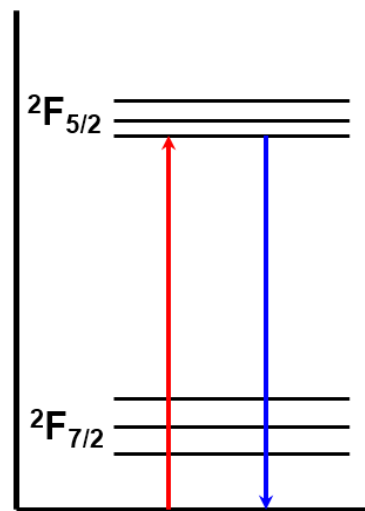


Figure 6. Schematic structure of the Stark levels of the ${}^2F_{7/2}$ and ${}^2F_{5/2}$ multiplets of Yb^{3+} ions.

Absorption spectra for the transition the main ${}^2F_{7/2}$ multiplet to the excited ${}^2F_{5/2}$ multiplet of Yb^{3+} ions were recorded for the 2Y0.8YbSZ, 2.5Y0.5YbSZ and 2.5Y0.7YbSZ crystals at $T = 77$ K. The spectrum of the cubic 10Y0.5NdSZ single crystal is shown for comparison.

Fragment of the ${}^2F_{7/2} \rightarrow {}^2F_{5/2}$ absorption spectra for Yb^{3+} ions of the test crystals corresponding to the transition between the bottom Stark components of the ${}^2F_{7/2}$ and ${}^2F_{5/2}$ multiplets of Yb^{3+} ions (red arrow in Figure 6) is shown in Figure 7.

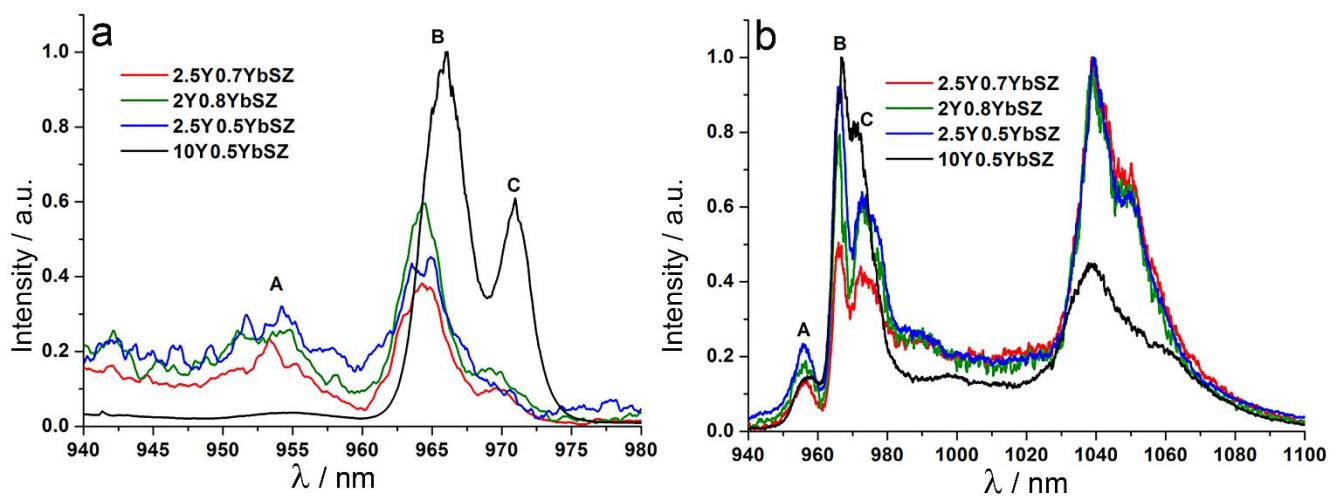


Figure 7. (a) ${}^2F_{7/2} \rightarrow {}^2F_{5/2}$ transition absorption spectra for Yb^{3+} ions and (b) ${}^2F_{5/2} \rightarrow {}^2F_{7/2}$ transition luminescence spectra for Yb^{3+} ions, $\lambda_{\text{ex}} = 907$ nm, $T = 300$ K, for 2Y0.8YbSZ, 2.5Y0.5YbSZ, 2.5Y0.7YbSZ and 10Y0.5YbSZ crystals.

The absorption spectra of the tetragonal crystals, by analogy with those for the cubic 10Y0.5YbSZ crystals, contain only three spectral bands marked as A, B and C. The band A is attributed to Yb^{3+} ions located in the centers of the eight-vertex stars and having a vacancy in the second coordination shell. The band C refers to Yb^{3+} ions located in the centers of the seven-vertex stars.

Comparison between the luminescence spectra of the 2Y0.8YbSZ, 2.5Y0.5YbSZ and 2.5Y0.7YbSZ tetragonal crystals and the stabilized 10Y0.5YbSZ zirconia crystal showed that the patterns of the spectra are close while having a number of differences. The tetragonal crystals exhibit a slight shift of the A and B band peaks towards shorter wavelengths relative to the respective peaks for the cubic zirconia crystal. The band C in the spectra of the tetragonal crystals has a more complex pattern as compared with that of the cubic crystal and contains at least two differently broadened bands.

The phase analysis data that indicate the presence the t and t' tetragonal phases in all the test tetragonal YYbSZ crystals suggest that the absorption and luminescence spectra of the 2Y0.8YbSZ, 2.5Y0.5YbSZ and 2.5Y0.7YbSZ crystals shown in Figure 7 are superpositions of the spectral bands A, B and C of Yb³⁺ ion optical centers that occupy positions in the t and t' phases.

Spectroscopic studies of the local crystalline structure of the rare-earth ions having small ionic radii ($R = \text{Er}^{3+}$, Yb^{3+}) in the YRSZ solid solutions suggest the following. The predominant factor controlling the formation of Er^{3+} and Yb^{3+} optical centers in the YErSZ and YYbSZ tetragonal solid solutions is the presence oxygen vacancies in the neighborhood of rare-earth ion. The Er^{3+} and Yb^{3+} ions occupy positions in the t and t' tetragonal phases. With an increase in the total concentration of stabilizing oxides, the fraction of the lower symmetry optical centers increases.

Thus optical spectroscopy studies showed that rare-earth ions of the beginning of the lanthanide series (Nd^{3+}) are mainly incorporated in the crystal lattice of the t' tetragonal phase. On the contrary ions of the end of the lanthanide series (Er^{3+} , Yb^{3+}) do not exhibit selectivity upon incorporation into t and t' phases.

Transmission electron microscopy study of the structure of the crystals showed that all the crystals contain twins (Figure 8). The morphology of the twins in the 2Y1.2RSZ crystals ($R = \text{Er}$, Yb , Tb and Sc) differed from those of the other crystals. The 2Y1.2RSZ specimens only contained small twins having quite homogeneous sizes, unlike other crystals that contained mixtures of large and small twins.

Twins form upon crystal cooling due to the transition from the single-phase cubic region to the two-phase region in accordance with the equilibrium phase diagrams. The stresses induced upon the cubic to tetragonal phase transition in the test crystals are mainly relieved by twinning rather than through dislocation formation. The twin creation completes at $\sim 1400^\circ\text{C}$ when the diffusion mobility of cations is negligible [27]. The phase transition temperature decreases with an increase in the stabilizing oxide concentration and hence the temperature range in which the twin structure forms becomes narrower. However the data presented in Figure 8 suggest that the type and sizes of the twins may depend on the substitution degree of stabilizing impurity cations (Y^{3+}) for doping impurity cations in the solid solution while retaining the total concentration of the introduced oxides at 3.2 mol.%. For example, twins in the 2.0Y1.2RSZ crystals are finer and more homogeneous in size than in the 2.5Y0.7RSZ crystals ($R = \text{Er}$, Yb and Tb), potentially attributable to the difference in the temperatures of the cubic to tetragonal phase transition in these crystals.

Table 2 shows the microhardness of the test crystals. The table shows the average values of microhardness according to the results of 25 measurements. The microhardness showed no anisotropy associated with the crystallographic orientation.

The data shown in Table 2 suggest that the microhardness increases with a decrease in the radius of the rare-earth element of the co-doping oxide: the highest microhardness was observed in the crystals co-doped with Yb_2O_3 .

No fracture toughness anisotropy was found in the 2Y1.2RSZ crystals ($R = \text{Tb}$, Er , Yb). The fracture toughness hardly depended on the crystallographic orientation of the specimen plane and varied but slightly (by less than 10%) for different indenter diagonal orientations in the specimen plane. For the 2Y1.2TbSZ, 2Y1.2ErSZ, 2Y1.2YbSZ and 2Y1.2ScSZ crystals, the fracture toughness was close: 6.5 ± 0.5 , 5.5 ± 0.5 , 5.5 ± 0.5 and $5.0 \pm 0.5 \text{ MPa}\cdot\text{m}^{1/2}$, respectively. The moderate fracture toughness of these crystals can be attributed to the relatively high content of the non-transformable tetragonal phase in these crystals ($\sim 30 \text{ vol.}\%$) in comparison with other crystals studied.

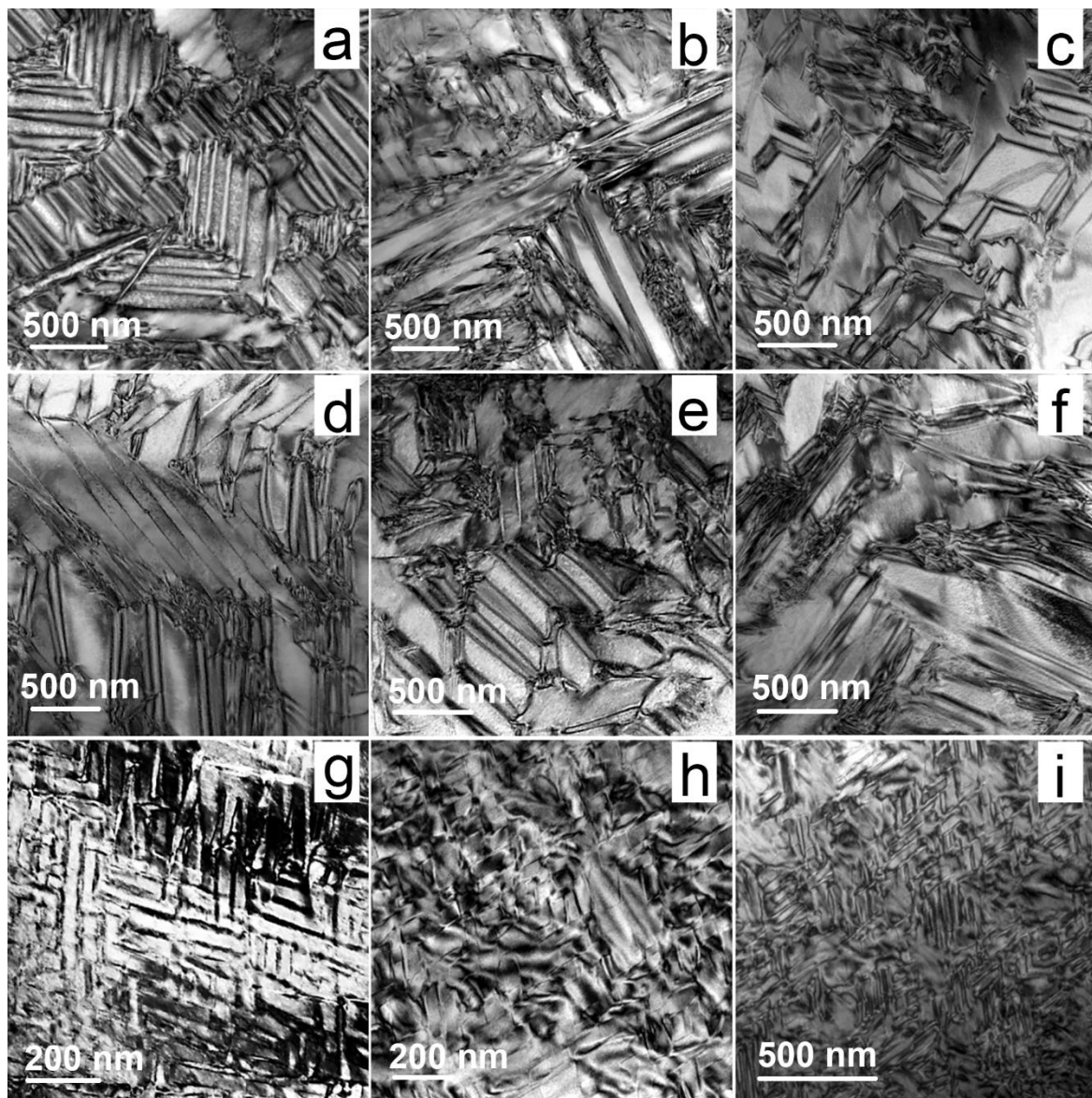


Figure 8. TEM images crystals: (a) 2.0Y0.8CeSZ, (b) 2.0Y0.8NdSZ, (c) 2.0Y0.8ErSZ, (d) 2.5Y0.7ErSZ, (e) 2.5Y0.7YbSZ, (f) 2.5Y0.7TbSZ, (g) 2.0Y1.2ErSZ, (h) 2.0Y1.2YbSZ and (i) 2.0Y1.2TbSZ crystals.

Table 2. Microhardness of the test crystals.

Specimen	Microhardness H, GPa				
	R = Ce	R = Nd	R = Tb	R = Er	R = Yb
2.0Y0.8RSZ	12.1 ± 0.5	12.2 ± 0.5	12.8 ± 0.5	13.0 ± 0.5	13.3 ± 0.5
2.5Y0.5RSZ	12.4 ± 0.5	12.5 ± 0.5	12.8 ± 0.5	13.2 ± 0.5	13.6 ± 0.5
2.5Y0.7RSZ	12.7 ± 0.5	12.9 ± 0.5	13.0 ± 0.5	13.5 ± 0.5	13.6 ± 0.5
2.0Y1.2RSZ	–	–	13.1 ± 0.5	13.7 ± 0.5	14.0 ± 0.5

Table 3 shows the fracture toughness for the 2Y0.8RSZ crystals (R = Ce, Nd, Tb, Er and Yb) for two indenter diagonal orientation in the specimen plane.

Table 3. Fracture toughness for 2Y0.8RSZ crystals (R = Ce, Nd, Tb, Er and Yb).

Diagonal Orientation	K_{Ic} , MPa·m ^{1/2}				
	R = Ce	R = Nd	R = Tb	R = Er	R = Yb
<100>	15.0 ± 0.5	10.2 ± 0.5	9.5 ± 0.5	8.5 ± 0.5	8.3 ± 0.5
<110>	10.5 ± 0.5	8.0 ± 0.5	8.0 ± 0.5	7.0 ± 0.5	7.0 ± 0.5

Analysis of the data in Table 3 showed a trend of increasing K_{Ic} with an increase in the radius of co-doping oxide cation. The highest fracture toughness of 15 MPa·m^{1/2} was observed in the 2Y0.8CeSZ crystals for the <100> orientation of the indenter diagonal. The data in Table 3 also suggest that the fracture toughness anisotropy is expressed to the greatest extent for the compositions having the highest fracture toughness, i.e., 2Y0.8CeSZ and 2Y0.8NdSZ.

Tables 4 and 5 show the fracture toughness for the 2.5Y0.5RSZ and 2.5Y0.7RSZ crystals (R = Ce, Nd, Tb, Er, Yb and Sc) for different indenter diagonal orientations in the specimen plane.

Table 4. Fracture toughness for the 2.5Y0.5RSZ and 2.5Y0.7RSZ crystals (R = Ce, Nd, Tb, Er, Yb and Sc).

Diagonal Orientation	K_{Ic} , MPa·m ^{1/2}				
	R = Ce	R = Nd	R = Tb	R = Er	R = Yb
<100>	10.0 ± 0.5	9.0 ± 0.5	8.5 ± 0.5	8.0 ± 0.5	7.5 ± 0.5
<110>	9.0 ± 0.5	8.0 ± 0.5	5.5 ± 0.5	6.0 ± 0.5	6.0 ± 0.5

Table 5. Fracture toughness for the 2.5Y0.7RSZ crystals (R = Ce, Nd, Tb, Er, Yb).

Diagonal Orientation	K_{Ic} , MPa·m ^{1/2}				
	R = Ce	R = Nd	R = Tb	R = Er	R = Yb
<100>	10.5 ± 0.5	9.0 ± 0.5	8.5 ± 0.5	7.5 ± 0.5	7.0 ± 0.5
<110>	9.5 ± 0.5	7.5 ± 0.5	6.5 ± 0.5	6.0 ± 0.5	6.5 ± 0.5

A change in the co-doping oxide concentration from 0.5 to 0.7 mol.% at a constant Y₂O₃ concentration of 2.5 mol.% did not cause any significant changes in the fracture toughness. The fracture toughness values of the 2.5Y0.5RSZ and 2.5Y0.7RSZ crystals for the same doping oxides were close.

The fracture toughness decreases in the 2.5Y0.5CeSZ → 2.5Y0.5NdSZ → 2.5Y0.5ErSZ → 2.5Y0.5YbSZ range of solid solutions. This trend is also observed in the 2.5Y0.7RSZ crystals (R = Ce, Nd, Er and Yb). The data in Tables 4 and 5 also suggest that an increase in the fracture toughness is accompanied by an increase in the fracture toughness anisotropy. Thus, the higher the fracture toughness of the crystals, the clearer the dependence of the fracture toughness on the crystallographic orientation of the specimens.

4. Summary

The phase composition, local crystal structure and mechanical properties of ZrO₂ crystals partially stabilized with Y₂O₃ and additionally doped with Nd₂O₃, CeO₂, Er₂O₃ and Tb₂O₃, Yb₂O₃ were studied. It is shown that the phase composition of crystals is determined mainly by the total concentration of stabilizing oxides and practically does not depend on the radius of the alloying cation. Study of the local crystal structure by time-resolution selective laser spectroscopy showed that rare-earth ions of the beginning of the lanthanide series (Nd³⁺) predominantly occupy positions in the non-transformable tetragonal phase of partially stabilized zirconia crystals. Ions of the end of the lanthanide series (Er³⁺, Yb³⁺) do not exhibit selectivity upon incorporation into the transformable (t) and the non-transformable (t') phases. Transmission electron microscopy study of the crystals showed that crystals of all the compositions contain twins. The sizes and habit

planes of the twins depend on the type and concentration of the stabilizing impurity. It is shown that at similar total doping oxide concentrations in the zirconia-based solid solution, the twin sizes depend on the substitution degree of Y^{3+} cations for rare-earth element cations. Study of the mechanical properties of the crystals, i.e., fracture toughness and microhardness, showed that the microhardness of the crystals increases with a decrease in the radius of the co-doping rare-earth cation: the highest microhardness was observed in the crystals co-doped with Yb_2O_3 . The fracture toughness of the crystals increases with an increase in the cation radius of the co-doping oxide. For the composition range studied, the highest fracture toughness of $15 \text{ MPa}\cdot\text{m}^{1/2}$ was observed for the $2Y0.8CeSZ$ specimens in the $\{100\}$ plane for the $\langle 100 \rangle$ orientation of the indenter diagonals. It is established that the higher fracture toughness of the crystals the more clearly the dependence of the fracture toughness on the crystallographic orientation of the specimens.

Author Contributions: Conceptualization, E.E.L. and N.Y.T.; Formal analysis, V.A.M.; Investigation, A.V.K., A.S.C., F.O.M., V.A.M., N.V.S.; Methodology, P.A.R.; Supervision, E.E.L.; Validation, P.A.R. and N.Y.T.; Visualization, A.V.K. and F.O.M.; Writing—review and editing, M.A.B., E.E.L., P.A.R. and N.Y.T. All authors have read and agreed to the published version of the manuscript.

Funding: The work was supported by the Ministry of Science and Higher Education of the Russian Federation as a part of the State Assignment (basic research, Project No. FSME-2020-0031 (0718-2020-0031). The study used the equipment from the Centre for collective use “Material Science and Metallurgy” of the NUST “MISIS” (agreement No. 075-15-2021-696).

Informed Consent Statement: Informed consent was obtained from all subjects involved in the study.

Conflicts of Interest: The authors declare no conflict of interest.

References

1. Chevalier, J.; Liens, A.; Reveron, H.; Zhang, F.; Reynaud, P.; Douillard, T.; Preiss, L.; Sergo, V.; Lughi, V.; Swain, M. Forty Years after the Promise of “Ceramic Steel”: Zirconia-Based Composites with a Metal-like Mechanical Behavior. *J. Am. Ceram. Soc.* **2019**, *103*, 1482–1513. [\[CrossRef\]](#)
2. Sabzi, M.; Dezfuli, S.M.; Balak, Z. Crystalline Texture Evolution, Control of the Tribocorrosion Behavior, and Significant Enhancement of the Abrasion Properties of a Ni-P Nanocomposite Coating Enhanced by Zirconia Nanoparticles. *Int. J. Miner. Metall. Mater.* **2019**, *26*, 1020–1030. [\[CrossRef\]](#)
3. Kazemi, F.; Arianpour, F.; Taheri, M.; Saberi, A.; Rezaie, H.R. Effects of Chelating Agents on the Sol-Gel Synthesis of Nano-Zirconia: Comparison of the Pechini and Sugar-Based Methods. *Int. J. Miner. Metall. Mater.* **2020**, *27*, 693–702. [\[CrossRef\]](#)
4. Peng, E.; Wei, X.; Garbe, U.; Yu, D.; Edouard, B.; Liu, A.; Ding, J. Robocasting of Dense Yttria-Stabilized Zirconia Structures. *J. Mater. Sci.* **2018**, *53*, 247–273. [\[CrossRef\]](#)
5. Li, Q.; Hao, X.; Gui, Y.; Qiu, H.; Ling, Y.; Zheng, H.; Omran, M.; Gao, L.; Chen, J.; Chen, G. Controlled Sintering and Phase Transformation of Yttria-Doped Tetragonal Zirconia Polycrystal Material. *Ceram. Int.* **2021**, *47*, 27188–27194. [\[CrossRef\]](#)
6. Piconi, C.; Maccauro, G. Zirconia as a Ceramic Biomaterial. *Biomaterials* **1999**, *20*, 1–25. [\[CrossRef\]](#)
7. Da, X.; Zou, D.; Chen, X.; Qiu, M.; Ke, W.; Fan, Y. Influence of Compatibility between Sol and Intermediate Layer on the Performance of Yttria-Stabilized Zirconia Nanofiltration Membrane. *Ceram. Int.* **2021**, *47*, 22801–22809. [\[CrossRef\]](#)
8. Basu, B.; Vleugels, J.; van der Biest, O. Microstructure–Toughness–Wear Relationship of Tetragonal Zirconia Ceramics. *J. Eur. Ceram. Soc.* **2004**, *24*, 2031–2040. [\[CrossRef\]](#)
9. Kalinina, M.V.; Fedorenko, N.Y.; Arsent’ev, M.Y.; Tikhonov, P.A.; Shilova, O.A. Obtaining ZrO_2 –3 Mol % Y_2O_3 Ceramics with Various Degrees of Tetragonality and Studying Low Temperature Degradation. *Glass Phys. Chem.* **2021**, *47*, 382–389. [\[CrossRef\]](#)
10. Singh, R.; Gill, C.; Lawson, S.; Dransfield, G.P. Sintering, Microstructure and Mechanical Properties of Commercial Y-TZPs. *J. Mater. Sci.* **1996**, *31*, 6055–6062. [\[CrossRef\]](#)
11. Zhang, F.; Vanmeensel, K.; Inokoshi, M.; Batuk, M.; Hadermann, J.; van Meerbeek, B.; Naert, I.; Vleugels, J. 3Y-TZP Ceramics with Improved Hydrothermal Degradation Resistance and Fracture Toughness. *J. Eur. Ceram. Soc.* **2014**, *34*, 2453–2463. [\[CrossRef\]](#)
12. Presenda, Á.; Salvador, M.D.; Moreno, R.; Borrell, A. Hydrothermal Degradation Behavior of Y-TZP Ceramics Sintered by Nonconventional Microwave Technology. *J. Am. Ceram. Soc.* **2015**, *98*, 3680–3689. [\[CrossRef\]](#)
13. Ramesh, S.; Zulkifli, N.; Tan, C.Y.; Wong, Y.H.; Tarlochan, F.; Ramesh, S.; Teng, W.D.; Sopyan, I.; Bang, L.T.; Sarhan, A.A.D. Comparison between Microwave and Conventional Sintering on the Properties and Microstructural Evolution of Tetragonal Zirconia. *Ceram. Int.* **2018**, *44*, 8922–8927. [\[CrossRef\]](#)
14. Sutharsini, U.; Thanihaichelvan, M.; Ting, C.H.; Ramesh, S.; Tan, C.Y.; Chandran, H.; Sarhan, A.A.D.; Ramesh, S.; Urriés, I. Effect of Two-Step Sintering on the Hydrothermal Ageing Resistance of Tetragonal Zirconia Polycrystals. *Ceram. Int.* **2017**, *43*, 7594–7599. [\[CrossRef\]](#)

15. Smirnov, A.; Kurland, H.-D.; Grabow, J.; Müller, F.A.; Bartolomé, J.F. Microstructure, Mechanical Properties and Low Temperature Degradation Resistance of 2Y-TZP Ceramic Materials Derived from Nanopowders Prepared by Laser Vaporization. *J. Eur. Ceram. Soc.* **2015**, *35*, 2685–2691. [[CrossRef](#)]
16. Upadhyaya, D.D.; Ghosh, A.; Dey, G.K.; Prasad, R.; Suri, A.K. Microwave Sintering of Zirconia Ceramics. *J. Mater. Sci.* **2001**, *36*, 4707–4710. [[CrossRef](#)]
17. Tsukuma, K.; Ueda, K.; Shimada, M. Strength and Fracture Toughness of Isostatically Hot-Pressed Composites of Al₂O₃ and Y₂O₃-Partially-Stabilized ZrO₂. *J. Am. Ceram. Soc.* **1985**, *68*, C-4–C-5. [[CrossRef](#)]
18. Ramesh, S.; Khan, M.M.; Alexander Chee, H.C.; Wong, Y.H.; Ganesan, P.; Kutty, M.G.; Sutharsini, U.; Chew, W.J.K.; Niakan, A. Sintering Behaviour and Properties of Graphene Oxide-Doped Y-TZP Ceramics. *Ceram. Int.* **2016**, *42*, 17620–17625. [[CrossRef](#)]
19. Kanellopoulos, P.; Gill, C. Hydrothermal Ageing of Yttria-Stabilised Zirconia, Sintered at 1300 °C–1325 °C: The Effects of Copper Oxide Doping and Sintering Time Variations. *J. Mater. Sci.* **2002**, *37*, 5075–5082. [[CrossRef](#)]
20. Ramesh, S.; Meenaloshini, S.; Tan, C.Y.; Chew, W.J.K.; Teng, W.D. Effect of Manganese Oxide on the Sintered Properties and Low Temperature Degradation of Y-TZP Ceramics. *Ceram. Int.* **2008**, *34*, 1603–1608. [[CrossRef](#)]
21. Michel, D.; Mazerolles, L.; Perez, Y.; Jorba, M. Fracture of Metastable Tetragonal Zirconia Crystals. *J. Mater. Sci.* **1983**, *18*, 2618–2628. [[CrossRef](#)]
22. Ingel, R.P.; Iii, D.L. Lattice Parameters and Density for Y₂O₃-Stabilized ZrO₂. *J. Am. Ceram. Soc.* **1986**, *69*, 325–332. [[CrossRef](#)]
23. Ingel, R.P.; Rice, R.W.; Lewis, D. Room-Temperature Strength and Fracture of ZrO₂-Y₂O₃ Single Crystals. *J. Am. Ceram. Soc.* **1982**, *65*, c108–c109. [[CrossRef](#)]
24. Osiko, V.V.; Borik, M.A.; Lomonova, E.E. Synthesis of Refractory Materials by Skull Melting Technique. In *Springer Handbook of Crystal Growth*; Springer: Berlin/Heidelberg, Germany, 2010; pp. 433–477.
25. Borik, M.A.; Bublik, V.T.; Kulebyakin, A.V.; Lomonova, E.E.; Milovich, F.O.; Myzina, V.A.; Osiko, V.V.; Seryakov, S.V.; Tabachkova, N.Y. Change in the Phase Composition, Structure and Mechanical Properties of Directed Melt Crystallised Partially Stabilised Zirconia Crystals Depending on the Concentration of Y₂O₃. *J. Eur. Ceram. Soc.* **2015**, *35*, 1889–1894. [[CrossRef](#)]
26. Voron'Ko, Y.K.; Vishnyakova, M.A.; Lomonova, E.E.; Popov, A.V.; Sobol', A.A.; Ushakov, S.N.; Shukshin, V.E. Spectroscopy of Yb³⁺ in Cubic ZrO₂ Crystals. *Inorg. Mater.* **2004**, *40*, 502–508. [[CrossRef](#)]
27. Kilo, M.; Taylor, M.A.; Argirusis, C.; Borchardt, G.; Lesage, B.; Weber, S.; Scherrer, S.T.; Schroeder, M.; Martin, M. Cation Self-Diffusion of ⁴⁴Ca, ⁸⁸Y and ⁹⁶Zr in Single Crystalline Calcia- and Yttria-Doped Zirconia. *J. Appl. Phys.* **2003**, *94*, 7547–7552. [[CrossRef](#)]